

NANO EXPRESS

Open Access



# Anisotropic Phase Transformation in B2 Crystalline CuZr Alloy

Shayuan Weng<sup>1</sup>, Tao Fu<sup>1\*</sup> , Xianghe Peng<sup>1,2\*</sup> and Xiang Chen<sup>1,3</sup>

## Abstract

B2 phase copper-zirconium (CuZr) particles are often used as an enhancement agent to improve the toughness of metallic glass; however, the orientation dependence of its phase transformation behaviors under loading remains unclear. In this work, molecular dynamics simulation of uniaxial tension and compression of B2 phase CuZr along different crystallographic orientation are performed to investigate the orientation-related mechanical response and phase transformation mechanisms. It was found that the mechanical behavior of CuZr exhibits obvious tension/compression asymmetry, but their failure mode is mainly local amorphization. Three different phase transformation behaviors, B2→FCC, B2→BCT, and B2→HCP, were observed in tension and compression along [001], and tension along [110], respectively. The transformations are realized by lattice rotation (~5°), uniform deformation and separation between Cu and Zr atomic layers, respectively. Before failure by local amorphization, phase transformation region can be recovered after unloading, showing the superelasticity.

**Keywords:** B2 phase CuZr, Phase transformation, Molecular dynamics, Uniaxial loading, Anisotropic

## Introduction

Bulk metallic glasses (BMGs) have attracted considerable attention due to their excellent mechanical and physical properties, such as high strength, elasticity, high hardness combined with excellent corrosion resistance, etc. [1–4]. Nevertheless, they usually fail by catastrophic brittle fracture through localized shear bands [5, 6]. This shortcoming has been overcome to a certain extent in some CuZr-based bulk metallic glass composites (BMGCs) enhanced by ductile B2 phase CuZr particles [3, 7–11]. Moreover, some B2 crystalline CuZr precipitations would be inherently formed through the crystallization in CuZr glass under loading, and then undergo twinning and dislocation gliding, inducing the change in the mechanical properties of BMGs, as was found in the experiment [12]. To toughen BMGs with B2 phase CuZr precipitations and design high-performance BMGs, the deformation behaviors of B2 phase CuZr should be clarified firstly.

B2 phase CuZr is a kind of shape memory alloy that has the ability to recover its original shape under specific

thermo-mechanical conditions [13, 14], which is different from the traditional crystalline materials that take dislocation glide or twinning as the main deformation mechanism [15–17]. The first-principle calculation based on functional density theory can be used to study the adsorption process [18–20] and the interfacial property [21, 22], but cannot be applied to study the dynamic evolution of the phase transition behaviors due to the limitation of calculation scale. Molecular dynamics (MD) simulation is an effective method to study the mechanical properties and deformation behaviors of materials [23–31]. Sutrarakar and Mahapatra investigated the effects of cross-sectional dimensions and temperature on the phase transformation in Cu-Zr nanowire, as well as the tension-compression asymmetry by MD simulation [32–34], and obtained some valuable results. For instance, the initial B2 phase is transformed to a body-centered-tetragonal (BCT) phase by the nucleation and propagation of a {100} twinning plane. Amigo et al. used two kinds of potentials [35, 36] in their MD simulations to investigate the phase transformation behaviors, and found that one yields the martensitic transformation from B2 to BCT structure, while the other does not [13].

It is known that the anisotropy of crystals plays an important role in the deformation of materials. Different

\* Correspondence: futao@cqu.edu.cn; futao@cqu.edu.cn; xhpeng@cqu.edu.cn

<sup>1</sup>Department of Engineering Mechanics, Chongqing University, Chongqing 400044, China

Full list of author information is available at the end of the article

deformation mechanisms may play dominant roles during deformation when the load is applied along different crystal orientation [37]. For instance, perfect dislocation glide and twinning are the main deformation mechanisms for the nanoindentation on (001) and (111) surfaces of vanadium nitride (VN) with a cylindrical indenter [38, 39], respectively, showing obvious anisotropic plasticity. For BCC iron nanowire, the phase transformation shows an intricate dependence on the crystallographic orientation, along which the load is applied,  $\langle 001 \rangle$  oriented wire exhibits a BCC  $\rightarrow$  FCC transformation, but  $\langle 011 \rangle$  and  $\langle 111 \rangle$  oriented wire follows a BCC  $\rightarrow$  HCP transformation [40]. The atomic distribution array in B2 structure is analogous to that in a BCC structure, but there are two kinds of elements in B2 structure. The crystal orientation of the reinforcing particles in BMGs is usually scattered, thus loading direction should have different influences on the toughening effect of different particle. Thus, it is necessary to study the deformation behavior of the enhancement particles with loading along different orientations.

Uniaxial tension and compression, as two basic loading modes usually used to evaluate the fundamental mechanical properties of materials. In this work, a series of MD simulations of uniaxial tension and compression tests of B2 crystalline CuZr along [001], [110], and [111] orientations are conducted to explore the dependence of phase transformation on loading orientation and the tension and compression (T/C) asymmetry.

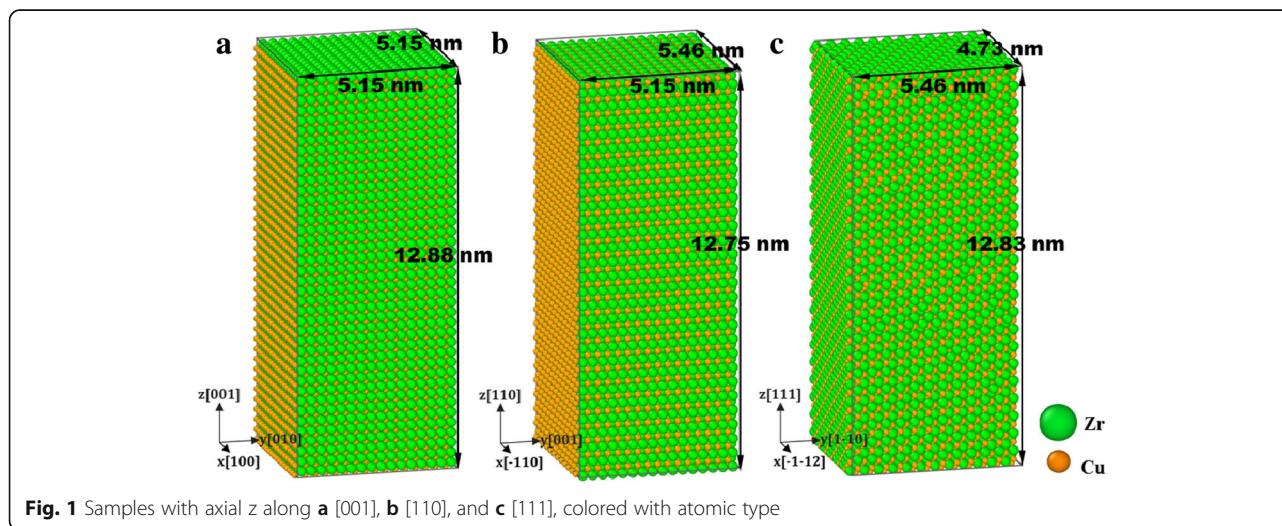
## Methods

The well-known embedded-atom method (EAM) [41] is selected to describe the interatomic force of Cu-Zr system. The EAM potential has been widely used to investigate the mechanical behavior of metals and their alloys [42–46]. Based on the frame of EAM, Mendeleev and his

colleagues have identified and optimized the potential parameters three times in 2007 [35], 2009 [36], and 2016 [47]. In this work, the parameters in the latest version of the interatomic potential for Cu-Zr [47] developed in 2016 are used. These parameters can yield more realistic stable and unstable stacking fault energy compared with that developed in 2009 [36], and can better describe the properties of crystalline CuZr.

Three samples with the loading axial  $z$  along the [001], [110], and [111] are prepared, respectively, as shown in Fig. 1. Before loading, a conjugate gradient (CG) algorithm is used to minimize the energy of the system to reach an optimized stable configuration. Mechanical tests are simulated at room temperature of 300 K. Then the system is relaxed with the isothermal-isobaric NPT ensemble at  $T = 300$  K for 20 ps to reach an equilibration state with pressure-free condition. It is found that the strain rate effect of nano-polycrystalline material becomes insignificant as the strain rate varies in the range between  $5 \times 10^8$  and  $1 \times 10^9$  s $^{-1}$ , therefore the strain rate is assigned as  $1 \times 10^9$  s $^{-1}$  by considering comprehensively both the accuracy and computation efficiency [48, 49]. Hence, each sample is stretched/compressed in the  $z$ -direction at a strain rate of  $10^9$  s $^{-1}$  during loading; meanwhile, the NPT ensemble with Nose/Hoover barostat is employed [50] to keep pressure free in  $x$ - and  $y$ -directions. In the relaxation and the loading stage, periodic boundary conditions are applied in  $x$ -,  $y$ -, and  $z$ -directions.

Common neighbor analysis (CNA) [51], an algorithm to characterize the local structural environment, is usually used as an effective method to classify the atoms in a crystalline system. The second nearest neighbor distance in a BCC structure is only 15% larger than the nearest one; therefore, CNA method would lose some reliability in the presence of strong thermal fluctuations and strain. To overcome this short, the polyhedral



template matching (PTM) method was proposed to classify the local structural environment of particles and identify the local crystalline structure of simple condensed phases (FCC, BCC, HCP, etc.) [52]. Compared with CNA [51], the PTM method promises greater reliability in the presence of strong thermal fluctuations and strain [52]. B2 and BCC structures have an analogous atomic arrangement; therefore, the identified BCC structure by this method is actually the B2 structure. After the local microstructure analysis for the data obtained by MD simulation with PTM, the atoms are colored according to the following rules: blue for BCC (B2) structure, green for FCC structure, red for stacking faults or HCP structure, purple for simple cubic (SC), and white for grain boundaries or dislocation cores. It should be noted that single layer, double layer, and continuous multilayer red atoms are represented as twin boundary, stacking fault, and HCP structure, respectively. Local regions containing red, green, blue, and white atoms are amorphous.

As a supplementary microstructure analysis method, the centro-symmetry parameter (CSP) is used to describe the local disorder [53]. For each atom, the CSP is calculated with the flowing formula:

$$\text{CSP} = \sum_{i=1}^{N/2} |\mathbf{R}_i + \mathbf{R}_{i+N/2}|^2, \quad (1)$$

where  $N = 12$  or  $8$  is the number of the first nearest-neighbors of a central atom in FCC or B2 structure, and

$\mathbf{R}_i$  and  $\mathbf{R}_{i+N/2}$  are the vectors from the central atom to a particular pair of the nearest neighbors. The CSP is zero for an atom whose nearest-neighbors are at their perfect lattice sites. If there is a defect such as a vacancy or dislocation in the vicinity of an atom, the CSP of the atom will become much larger than that caused by local atomic vibration. The open software Ovito developed by Stukowski [54] is utilized to display atomic configurations.

## Results and Discussions

### Stress-Strain Curves

Figure 2 shows the stress-strain ( $\sigma$ - $\epsilon$ ) curves for B2 phase CuZr subjected to uniaxial tension and compression along [001], [110], and [111]. It can be noted that the stress is larger than that by experiment [55], because (1) the time scale used in MD simulation differs from that used in experiment, resulting in a much larger indentation speed than that in experiment; and (2) the defects including point defect, dislocations, and grain boundaries etc. are not considered in the simulations. At the initial stage, these curves develop linearly and then show different trends. After the first peak, these curves can be divided into three groups. In group I, the curves drop rapidly to low levels of stress, such as compression along [110] and [111]. In group II, the stresses fall to a platform and fluctuate with the increase of strain after the first peak, such as tension along [001], [110] and compression along [001]. The curves then climb to their

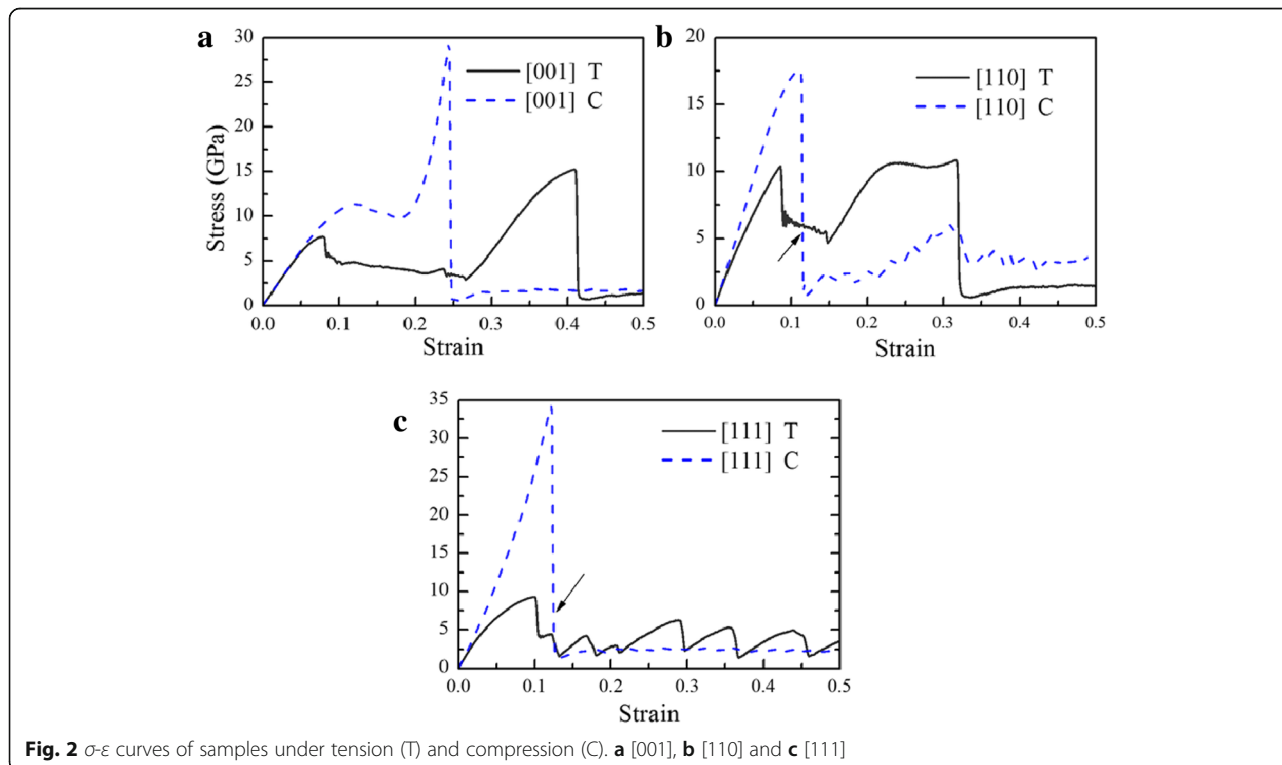


**Table 1**  $E$  of samples under tension and compression along different orientations

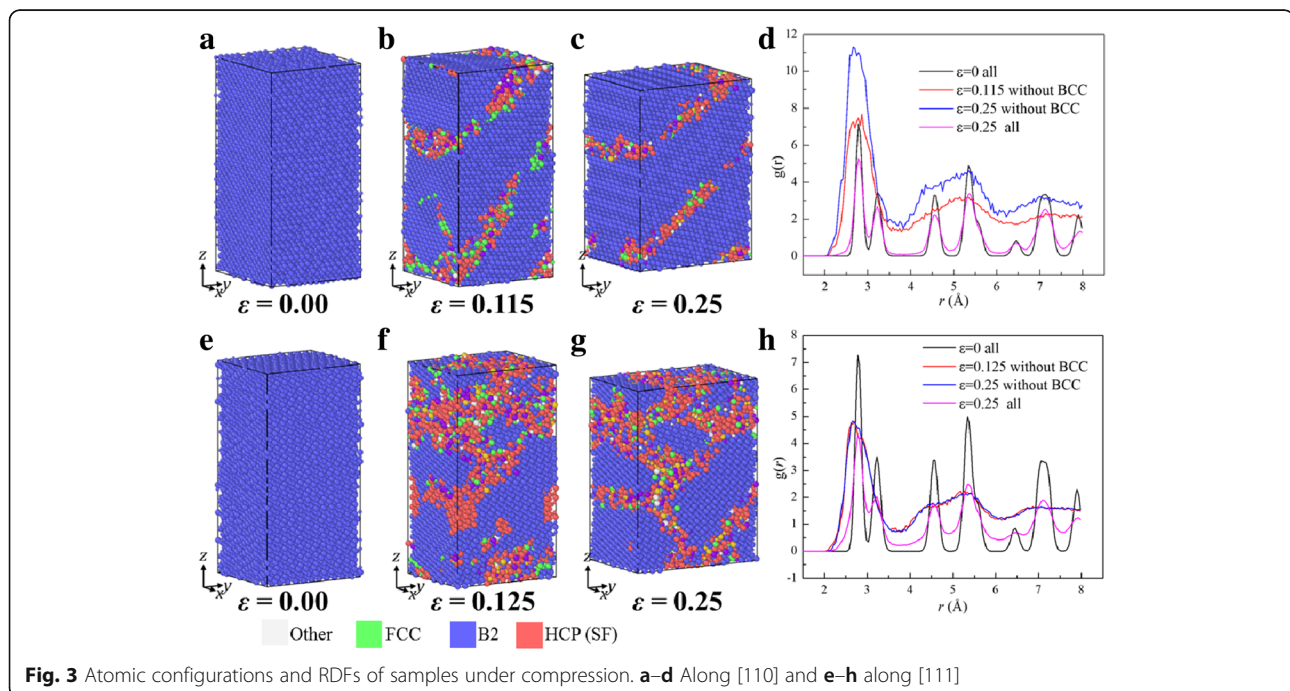
	$E_{[001]}$ (GPa)	$E_{[110]}$ (GPa)	$E_{[111]}$ (GPa)
Tension	125.68	150.09	160.99
Compression	124.97	176.23	199.97

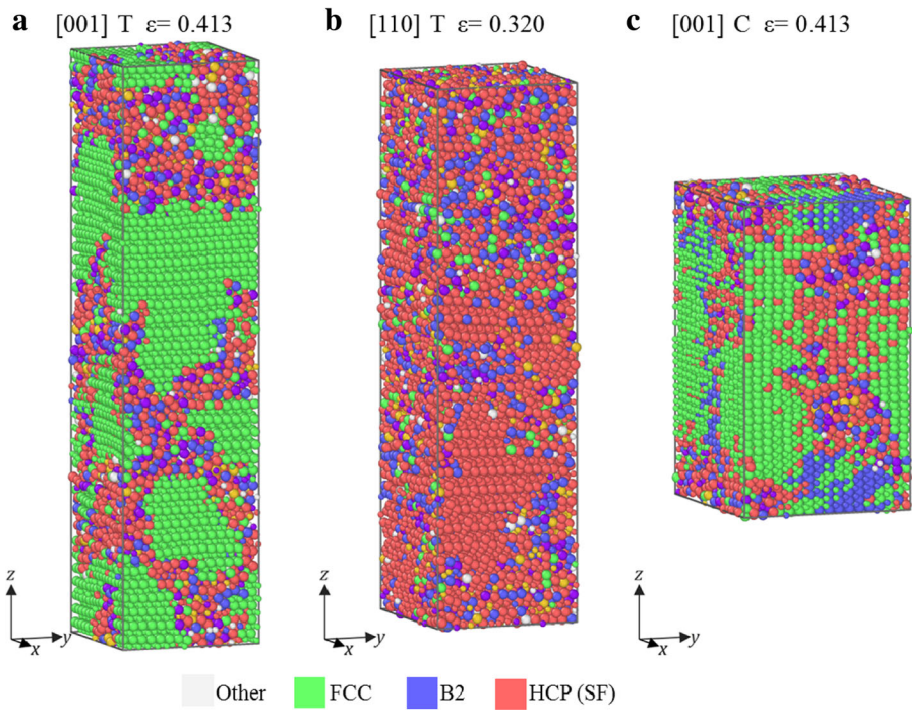
second peaks before final sharp drop. In group III, the curve drops rapidly to low levels of stress, and then fluctuates in a zigzag pattern, such as tension along [111]. Before the first peak, samples stay in the B2 structure and no obvious dislocation glide and twinning can be observed, which can be regarded as the elastic deformation. In the linear elastic stage, the Young's modulus  $E$  can be obtained by fitting the slope of each curve in the range of  $0.00 < \varepsilon < 0.02$ , and listed in Table 1, where it can be seen that the [001] orientation is the softest and [111] is the stiffest. This agrees with results of bulk BCC iron [40]. The  $E$  of the sample under compression is larger than that under tension except for [001] orientation, in consistency with that observed in Cu single crystal [56], which should be ascribed to the higher friction under compression [56]. The rest of curves at the elastic stage under compression deviate from that under tension obviously, which should be ascribed to the asymmetrical tensile and compressive nature of the interatomic potential [57]. After the first peak, it is unclear whether deformation should be attributed to dislocation slip or phase transformation; therefore, this region cannot be seen as inelastic or plastic T/C asymmetry, which differs with others' works [57–59]. In the

flowing section, the deformation mechanisms of the sample subjected to loadings along different directions will be discussed in details.

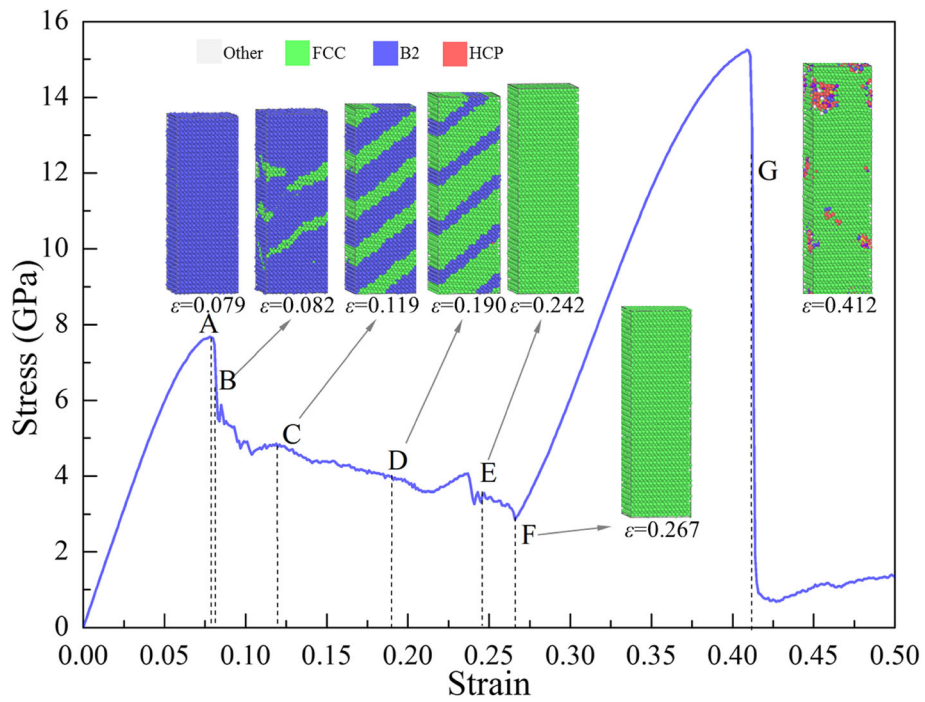
### Failure Behavior

Figure 3 shows the atomic structures and the radial distribution functions (RDFs) of the samples subjected to compression along [110] and [111], whose  $\sigma$ - $\varepsilon$  curves can be seen in Fig. 2 labeled as [110] C and [111] C. Figure 3a, d shows the initial samples [110] and [111] after relaxation at 300 K, where it can be seen that the atoms are in the B2 structure. When  $\varepsilon$  is increased to 0.115 or 0.125 for [110] C and [111] C, respectively, the region with mixed structures appears, as shown in Fig. 3b, f. The structure in the mixed area is defined as a mixed phase. The nucleation of mixed phase corresponds to the rapid drops stage of curves [110] C and [111] C in Fig. 2b, c, which is marked with arrows. Therefore, the transformation of local structure from B2 to a mixed phase causes the rapid drop of stress. In the flowing stage, the volume fraction variation of the mixed phase is the main mechanism to accommodate further deformation, the local structures in the samples under compression along [110] and [111] at  $\varepsilon = 0.25$  are shown in Fig. 3c, g, respectively. To specify the structure in the mixed region, the radial distribution function (RDFs),  $g(r)$ , of the samples under compression along [110] and [111] at different strains are shown in Fig. 3d, h. The peaks of the  $g(r)$  of the samples at  $\varepsilon = 0$  and  $\varepsilon = 0.25$  are sharp, indicating that they still maintain crystalline feature. While the peaks of the  $g(r)$  for the mixed regions, i.e.,





**Fig. 4** Atomic configurations in samples at failure strain. **a** Under tension along [001], **b** under tension along [110], and **c** under compression along [111]



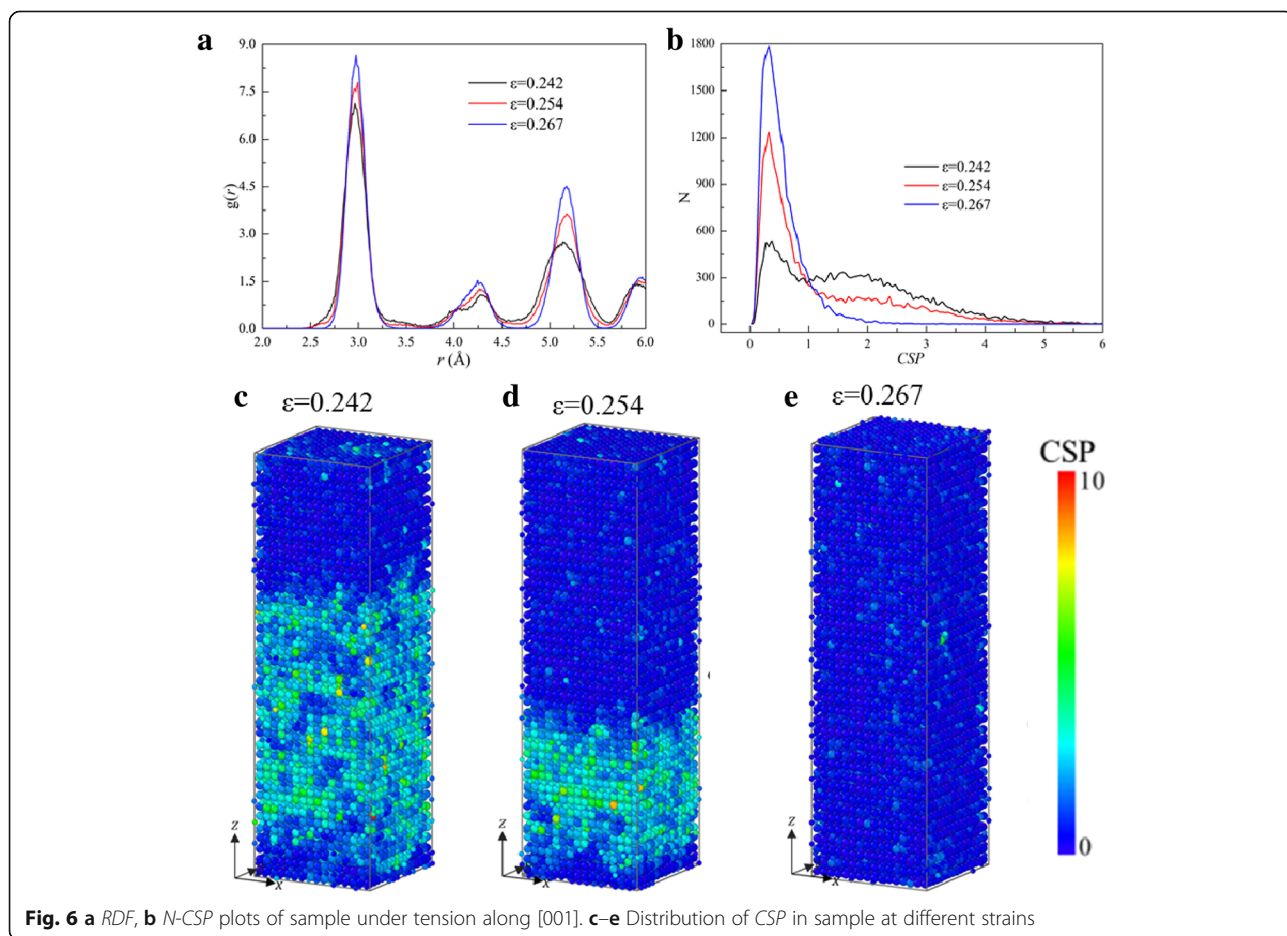
**Fig. 5**  $\sigma$ - $\epsilon$  curve of the sample under tension along [001], colored with local structure, with blue, green, and red representing B2, FCC, and amorphous phases, respectively

the sample without B2 regions, are blunt except the first ones, indicating that the mixed region is in an amorphous state. The dislocation extraction algorithm (DXA) [60] are also used to detect whether there is any dislocation nucleation, and find no obvious dislocations throughout the deformation process. Therefore, the amorphization of the B2 phase is conducted to be the main failure mode, resulting in the rapid drop, marked with arrows in Fig. 2b, c.

Figure 4 shows the atomic configurations after the rapid drop strain (failure strain) of the samples under tension along [001], [110] and compression along [001], whose  $\sigma$ - $\epsilon$  curves belong to group II. It can be seen in Fig. 4 that mixed regions form, similar to that in group I, indicating that amorphization is also the main failure mode (Fig. 4). However, these mixed regions are surrounded by green and red atoms (FCC and HCP structure), which is different from B2 structure in Fig. 3. This difference indicates that the mixed phase is transformed from B2 structure under compression in Fig. 3, but from FCC for sample [001] under tension and compression, and from HCP for sample [110] under tension.

### Phase Transformations

Figure 5 shows the  $\sigma$ - $\epsilon$  curve of the sample [001] under tension, where the microstructures at typical points (marked with A, B, ... , G) are also exhibited. The atoms at point A ( $\epsilon = 0.079$ ) are in B2 structure, indicating that before  $\epsilon = 0.079$  the deformation in the sample is elastic. However, local transformation from B2 to FCC takes place, as shown in the inset of  $\epsilon = 0.082$  in Fig. 5, resulting in the first rapid drop (A $\rightarrow$ B) to  $\epsilon = 0.082$ , where the release of the elastic energy stored due to the redistribution of the atomic configuration provides the energy for the need of the phase transformation. In the flowing stage of B $\rightarrow$ F, the elastic energy stored is further released as the phase transformation continues, leading to the reduction of stress. The local structure of the sample becomes FCC completely at  $\epsilon = 0.242$  (point E). And the structure keeps changed between Point E and F, but the stress keeps falling with the increase of strain. To reveal the change of microstructure, the distribution of  $g(r)$  and the variation of the number of atoms ( $N$ ) against CSP ( $N$ -CSP) of the sample at  $\epsilon = 0.242, 0.254,$  and  $0.267$  (between points E and F) are calculated and shown in Fig. 6a, b, respectively, where the height of each peak

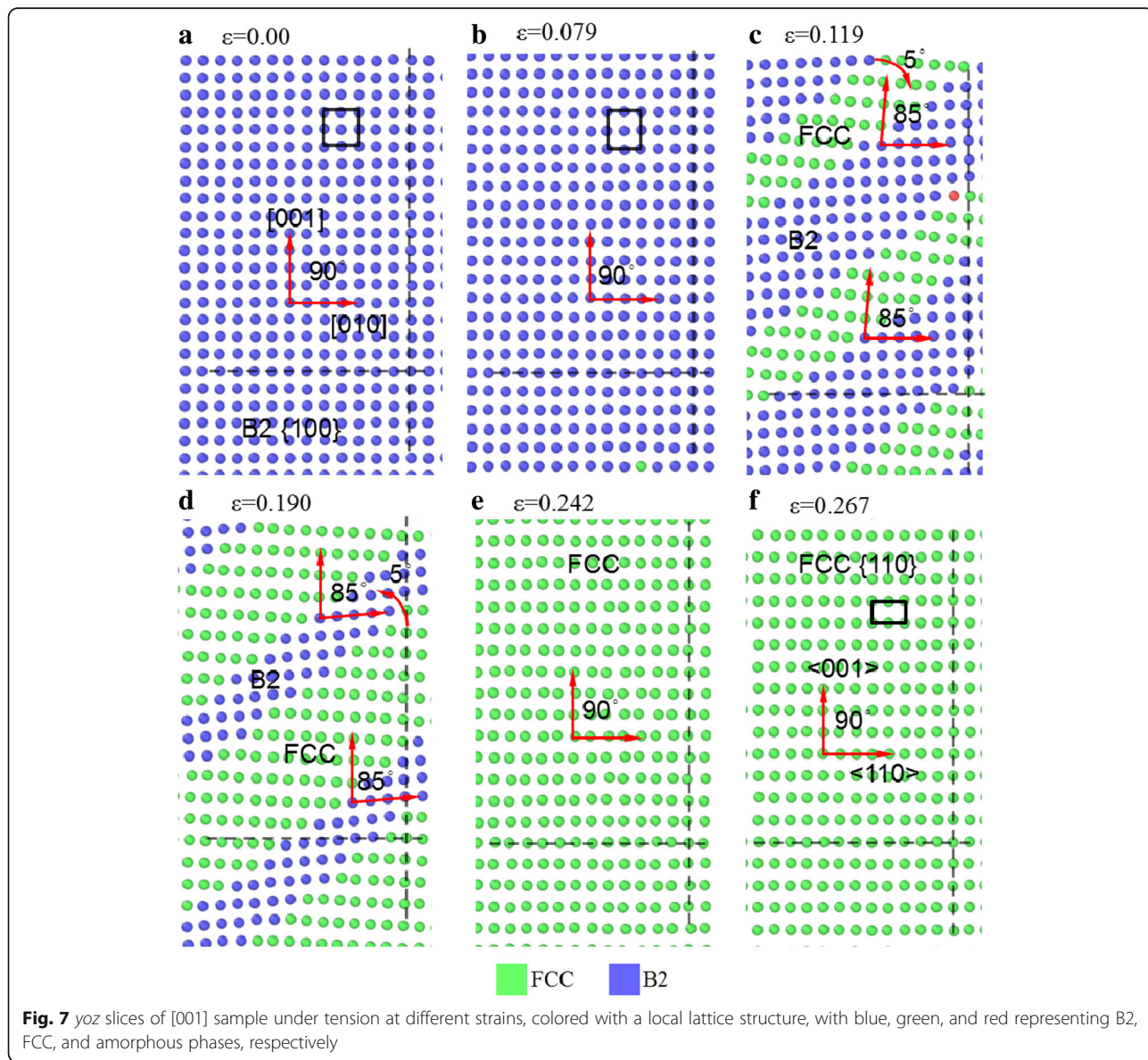


increase with the increase of strain, indicating that the system becomes more compact.

To characterize whether an atom is a part of a perfect lattice or a local defect, e.g., a dislocation or stacking fault, or a surface, the CSP [53] of the atoms with the number of nearest neighbors of FCC structure ( $N = 12$ ) are calculated, as shown in Fig. 6c–e. And larger CSP means a larger deviation from the perfect lattice [17]. It can be seen in Fig. 6b that the number of atoms with  $CSP < 1$  increase with the increase of strain, which can be also seen more intuitively from the distribution of CSPs of atoms in Fig. 6c–e. It differs from the common results that usually CSP would not decrease with the increase of strain. Therefore, the main deformation behaviors in this stage should also be attributed to the phase transformation from imperfect FCC to perfect FCC. In

the flowing stage, the sample with FCC structures is stretched, and stress will increase until reaching the second yield point. Then the curve drops sharply, corresponding to local amorphization rather than the nucleation of dislocation or slip.

To illustrate the phase transformation of the material during deformation, Fig. 7 shows some  $yoz$  slices of the sample [001] under tension at different strains. The horizontal and vertical dashed lines are used as references to identify whether the atomic structures rotate and deviate. With the increase of  $\epsilon$  from 0.0 to 0.079, the atoms lie on lines parallel to the horizontal and vertical axes, indicating that they are of B2 local structure. However, the atomic array in Fig. 7b changes to that in Fig. 7c as  $\epsilon$  from 0.079 to 0.119 when some B2 structures transform to the FCC structure. The angle between the arrays



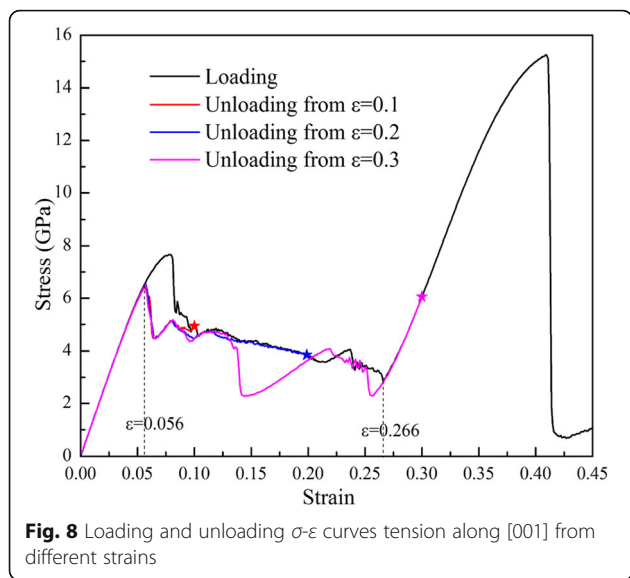


**Fig. 8** Loading and unloading  $\sigma$ - $\epsilon$  curves tension along [001] from different strains

changes from  $90^\circ$  in Fig. 7b for B2 structure to  $\sim 85^\circ$  in Fig. 7c for FCC structure with the lattice orientation deviating from the vertical axis by clockwise  $5^\circ$ , but the atomic array of B2 structure does not change obviously and has no obvious rotation. During  $0.119 < \epsilon < 0.190$ , the FCC area increases, and the array of green atoms gradually rotate counterclockwise. At  $\epsilon = 0.242$ , all the B2 structure transforms to FCC structures, as shown in Fig. 7e, where the three lattice orientations become nearly parallel with the three axes respectively, but there is still marked deviation, indicating the FCC structure is not perfect, which is in consistency with that shown in Fig. 6c. In the flowing stage, the atomic array tends regularly, as shown in Fig. 7f at  $\epsilon = 0.267$ , which is recognized as a {110} plane of FCC structure, with its crystal orientation in horizontal and vertical directions changed from [010] and [001] of B2 structure to  $\langle 110 \rangle$  and  $\langle 001 \rangle$  of FCC structure.

The simulation for the response of the sample (100) during unloading from different maximum tensile strains

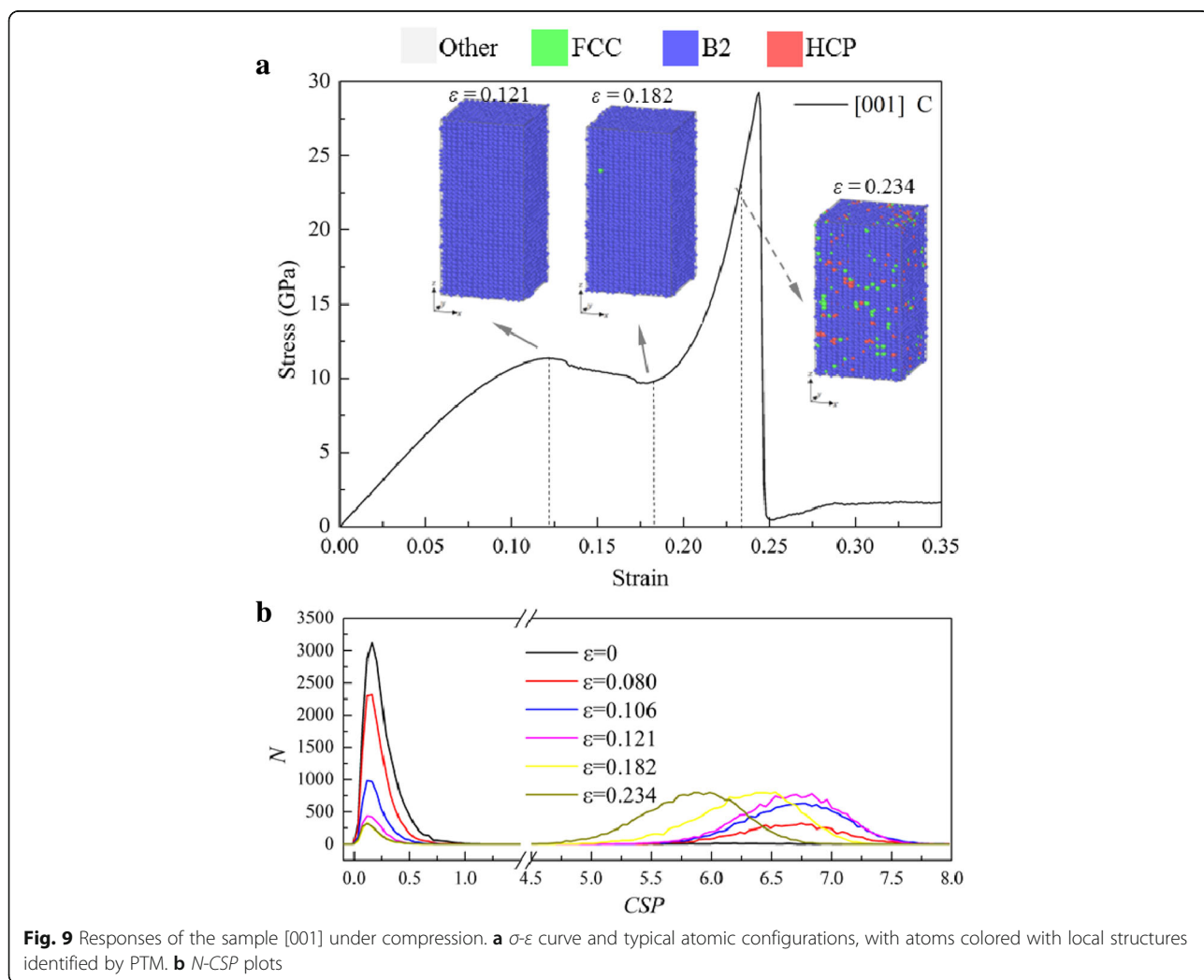
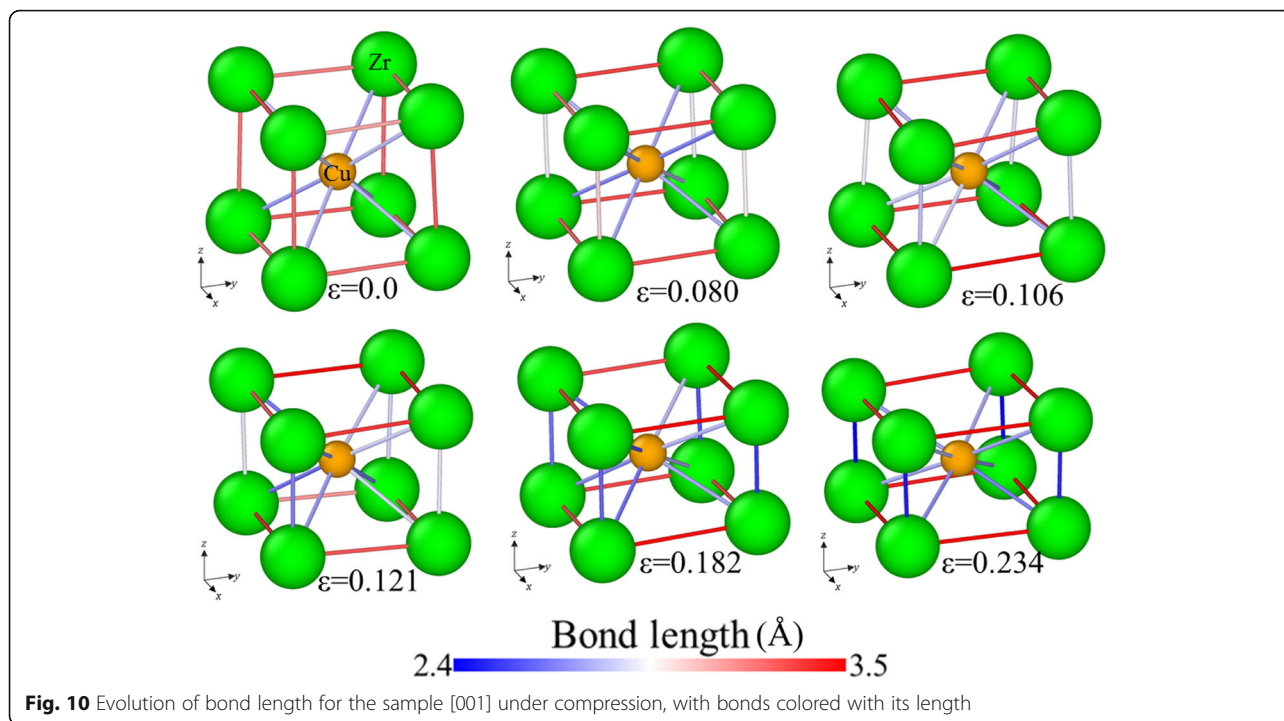


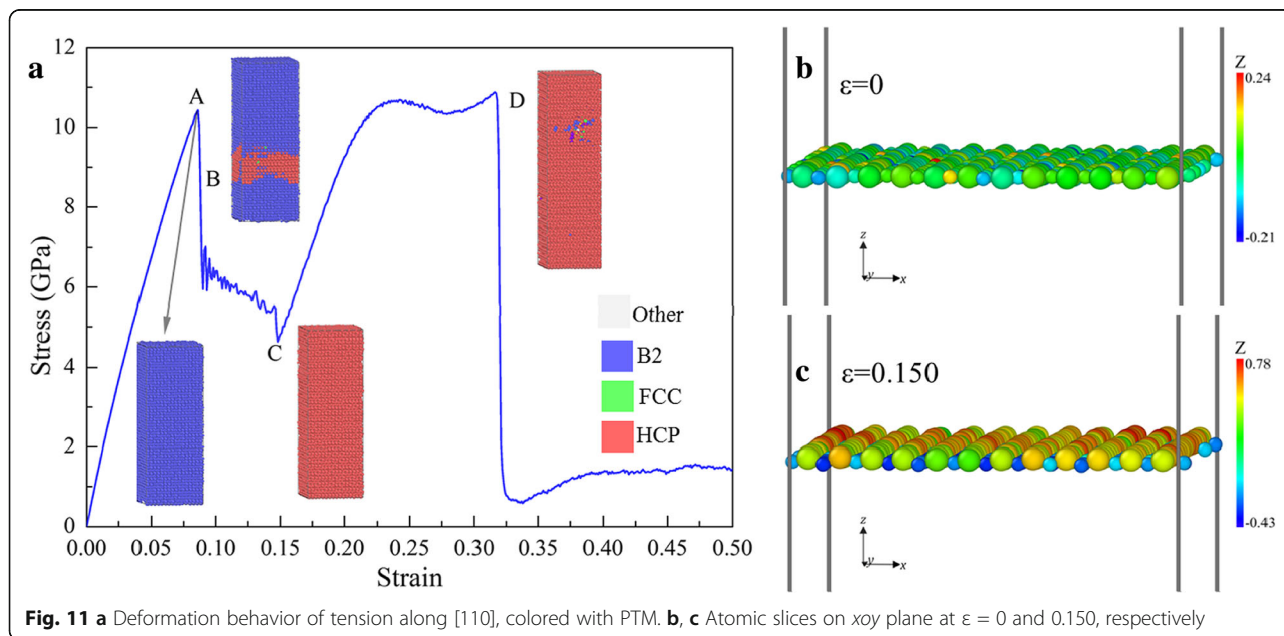
**Fig. 9** Responses of the sample [001] under compression. **a**  $\sigma$ - $\epsilon$  curve and typical atomic configurations, with atoms colored with local structures identified by PTM. **b**  $N$ -CSP plots



( $\epsilon_{\max} = 0.1, 0.2, \text{ and } 0.3$ , respectively) are performed, and the  $\sigma$ - $\epsilon$  curves are shown in Fig. 8. It can be seen that the unloading  $\sigma$ - $\epsilon$  curves between  $\epsilon = 0.266$  and  $\epsilon = 0.056$  do not overlap the loading curve, but they can meet with the elastic  $\sigma$ - $\epsilon$  curve at  $\epsilon = 0.056$  and then return to the origin along the elastic  $\sigma$ - $\epsilon$  curve, exhibiting the superelastic characteristic. The loading and unloading paths form hysteresis loops, which should be

ascribed to the different paths of forwarding and inverse phase transformations.

The  $\sigma$ - $\epsilon$  curve of the sample [001] under compression has a similar trend, as shown in Fig. 9a, which can be divided into four stages: (1)  $\sigma$  increases linearly with the increase of strain; (2)  $\sigma$  drops to a plateau; (3)  $\sigma$  increases linearly with a larger slope to the second peak as the increase of strain; (4)  $\sigma$  drops sharply to the second



plateau. By analyzing the local structures with PTM, one can find that most atoms are identified as B2 structure before reaching the second peak, except some scattered atoms that are identified as other local structure, as shown in Fig. 9a. However, according to the previous understanding, a sudden change in the  $\sigma$ - $\varepsilon$  curves usually corresponds to the change of microstructure. To further confirm it, the  $N$ -CSP plots are calculated and shown in Fig. 9b, in which the CSP for each atom at different strains is calculated with the nearest neighbors of the B2 structure ( $N = 8$ ). When  $\varepsilon = 0$ , the CSP of atoms is larger than 0, but less than 1, due to the effect of temperature, implying that the atoms are in perfect B2 structure. With the increase of  $\varepsilon$ , the atoms can be divided into two groups by their CSPs:  $CSP < 1$  and  $5 < CSP < 7.5$ . At  $0.080 < \varepsilon < 0.121$ , the CSPs at the second peaks are the same, but the number of atoms in this CSP range increases and tends stable, indicating the formation of new phases or defects (such as stacking fault). The CSP at the second peak decreases with the further increase of  $\varepsilon$ , i.e., the second wave moves leftwards. Figure 10 shows the evolution of bond length in a unit cell at different strains. At  $\varepsilon = 0$ , eight Cu atoms at the vertices and one Zr atom at the body-center make up the B2 structure. The relationship between the lattice parameters is  $a = b = c$ . With the increase of  $\varepsilon$ , the length of the bond in  $xoy$  plane increases, but that in  $xoz$  plane decreases. By calculating the strain in the other two directions during loading, one can find that the strains in the other two directions are identical before the second peaks. Therefore, the lengths of the bonds along  $x$ - and  $y$ -directions should be identical, and larger than that along the  $z$ -direction. The relationship between lattice parameters becomes  $a = b > c$ . These arrays of atoms can be recognized as BCT structure. In conclusion, the transformation from a B2 structure to BCT structure is the main deformation mechanism for sample [001] under compression.

Figure 11a shows the response of the sample [110] under tension. The first peak (point A) corresponds to the yield limit of the B2 structure, then some local B2 structure transforms to the HCP structure, resulting in the sharp drop. With the increase of  $\varepsilon$ , the stress decreases until point C when the sample is transformed totally to HCP. Figure 11b, c is the  $xoy$  one-layer slices at  $\varepsilon = 0$  and 0.150, respectively, where one can see that at the initial stage the Cu and Zr atoms are in an identical atomic layer (Fig. 11b). However, Cu and Zr atoms are separated into adjacent layers at  $\varepsilon = 0.150$  (Fig. 11c), which results in the phase transformation from B2 to HCP. Then with the increase of  $\varepsilon$ ,  $\sigma$  increases with a smaller slope than that in the initial linear stage until point D, followed by a sharp fall to a low stress level, corresponding to failure due to local amorphization.

## Conclusions

In this work, the responses and phase transformation of CuZr samples subjected to uniaxial tension and compression along [001], [110], [111] orientations are studied respectively using molecular dynamics simulations, making use of the latest interatomic potential, from which the following main conclusions can be drawn:

1. The mechanical responses of the CuZr samples under tension and under compression exhibit obvious asymmetry, and their main failure mechanism should be local amorphization.
2. There are three kinds of phase transformations: B2→FCC, B2→BCT, and B2→HCP in tension and compression along [001], and tension along [110].
3. B2→FCC, B2→BCT, and B2→HCP phase transformations are found to be realized by unique mechanisms respectively which are lattice rotation ( $\sim 5^\circ$ ), uniform deformation and separation from Cu and Zr atomic layer for each.
4. Phase transformation region can be recovered after unloading before local amorphization, showing the superelasticity.

The results are important for the exploration of the mechanical properties and deformation mechanisms of nanocrystalline CuZr, and for the applications of nanocrystalline CuZr particles as an enhancement agent to improve the toughness of metallic glass.

## Abbreviations

BCC: Body-centered cubic; BCT: Body-centered-tetragonal; BMG: Bulk metallic glasses; BMGC: Bulk metallic glass composites; CG: Conjugate gradient; CNA: Common neighbor analysis; CSP: Centro-symmetry parameter; Cu: Copper; CuZr: Copper-zirconium; DXA: Dislocation extraction algorithm; EAM: Embedded-atom method; FCC: Face-centered cubic; HCP: Hexagonal close-packed; MD: Molecular dynamics; NPT: Constant number of particles, pressure, and temperature; PTM: Polyhedral template matching; RDF: Radial distribution function; T/C: Tension and compression; VN: Vanadium nitride; Zr: Zirconium;  $\varepsilon$ : Strain;  $\sigma$ : Stress

## Acknowledgements

MD simulations were carried out at Supercomputing Center of Lv Liang Cloud Computing Center in China.

## Authors' Contributions

TF and SW designed the scheme and wrote the manuscript under the guidance of XP. TF, XC, and SW performed the calculations and analyzed the results. XC participated in the discussions, and provided valuable suggestions. All authors read and approved the final manuscript.

## Funding

The authors acknowledge the financial supports from the National Natural Science Foundation of China (grant nos. 11802045, 11332013 and 11802047), the Postdoctoral Program for Innovative Talents of Chongqing (grant no. CQBX201804), and the China Postdoctoral Science Foundation (grant nos. 2018M631058 and 2019T120804).

## Availability of Data and Materials

The datasets used or analyzed during the current study are available from the corresponding author on reasonable request.

**Competing Interests**

The authors declare that they have no competing interests.

**Author details**

<sup>1</sup>Department of Engineering Mechanics, Chongqing University, Chongqing 400044, China. <sup>2</sup>State Key Laboratory of Coal Mine Disaster Dynamics and Control, Chongqing University, Chongqing 400044, China. <sup>3</sup>Advanced Manufacturing Engineering, Chongqing University of Posts and Telecommunications, Chongqing 400065, China.

Received: 13 June 2019 Accepted: 1 August 2019

Published online: 16 August 2019

**References**

- Zhao L, Chan KC, Chen SH (2018) Atomistic deformation mechanisms of amorphous/polycrystalline metallic nanolaminates. *Intermetallics* 95:102–109
- Sun HC, Ning ZL, Wang G, Liang WZ, Pauly S, Huang YJ, Guo S, Xue X, Sun JF (2018) In-situ tensile testing of ZrCu-based metallic glass composites. *Scientific reports* 8:4651
- Liu ZQ, Li R, Liu G, Su WH, Wang H, Li Y, Shi MJ, Luo XK, Wu GJ, Zhang T (2012) Microstructural tailoring and improvement of mechanical properties in CuZr-based bulk metallic glass composites. *Acta Materialia* 60:3128–3139
- Cui Y, Abad OT, Wang F, Huang P, Lu TJ, Xu KW, Wang J (2016) Plastic Deformation Modes of CuZr/Cu Multilayers. *Scientific reports* 6:23306
- Liu YJ, Yao HW, Zhang TW, Wang Z, Wang YS, Qiao JW, Yang HJ, Wang ZH (2017) Designing ductile CuZr-based metallic glass matrix composites. *Mat Sci Eng a-Struct* 682:542–549
- Pauly S, Gorantla S, Wang G, Kuhn U, Eckert J (2010) Transformation-mediated ductility in CuZr-based bulk metallic glasses. *Nature materials* 9: 473–477
- Hofmann, D.C., (2010) Materials science. Shape memory bulk metallic glass composites, *Science*, 329: 1294–1295.
- Song KK, Pauly S, Zhang Y, Li R, Gorantla S, Narayanan N, Kuhn U, Gemming T, Eckert J (2012) Triple yielding and deformation mechanisms in metastable Cu<sub>47.5</sub>Zr<sub>47.5</sub>Al<sub>5</sub> composites. *Acta Materialia* 60:6000–6012
- Wei R, Chen LB, Li HP, Li FS (2017) Compression-compression fatigue behavior of CuZr-based bulk metallic glass composite containing B2 phase. *Intermetallics* 85:54–58
- Song KK, Pauly S, Zhang Y, Gargarella P, Li R, Barekar NS, Kuhn U, Stoica M, Eckert J (2011) Strategy for pinpointing the formation of B2 CuZr in metastable CuZr-based shape memory alloys. *Acta Materialia* 59:6620–6630
- Sepulveda-Macias M, Amigo N, Gutierrez G (2018) Tensile behavior of Cu<sub>50</sub>Zr<sub>50</sub> metallic glass nanowire with a B2 crystalline precipitate. *Physica B-Condensed Matter* 531:64–69
- Hajlaoui K, Alsaleh N, Alrasheedi NH, Yavari AR (2017) Coalescence and subsequent twinning of nanocrystals during deformation of CuZr-based metallic glasses: The grain size effect. *J Non-Cryst Solids* 464:39–43
- Amigo N, Sepulveda-Macias M, Gutiérrez G (2017) Martensitic transformation to monoclinic phase in bulk B2–CuZr. *Intermetallics* 91:16–21
- Chen X, Lu S, Zhao Y, Fu T, Huang C, Peng XH (2018) Molecular dynamic simulation on nano-indentation of NiTi SMA. *Mat Sci Eng a-Struct* 712:592–602
- Weng S, Ning H, Fu T, Hu N, Zhao Y, Huang C, Peng X (2018) Molecular dynamics study of strengthening mechanism of nanolaminated graphene/Cu composites under compression. *Scientific reports* 8:3089
- Weng S, Ning H, Hu N, Yan C, Fu T, Peng X, Fu S, Zhang J, Xu C, Sun D, Liu Y, Wu L, (2016) Strengthening effects of twin interface in Cu/Ni multilayer thin films – A molecular dynamics study, *Mater Des*, 111: 1–8.
- Fu T, Peng XH, Wang C, Lin ZJ, Chen XS, Hu N, Wang ZC (2017) Molecular dynamics simulation of plasticity in VN(001) crystals under nanoindentation with a spherical indenter. *Applied Surface Science* 392:942–949
- Gui YG, Tang C, Zhou Q, Xu LN, Zhao ZY, Zhang XX (2018) The sensing mechanism of N-doped SWCNTs toward SF<sub>6</sub> decomposition products: A first-principle study. *Applied Surface Science* 440:846–852
- Liu D, Gui Y, Ji C, Tang C, Zhou Q, Li J, Zhang X (2019) Adsorption of SF<sub>6</sub> decomposition components over Pd (1 1 1): A density functional theory study. *Applied Surface Science* 465:172–179
- Wang Y, Gui Y, Ji C, Tang C, Zhou Q, Li J, Zhang X (2018) Adsorption of SF<sub>6</sub> decomposition components on Pt<sub>3</sub>-TiO<sub>2</sub>(1 0 1) surface: A DFT study. *Applied Surface Science* 459:242–248
- Liu X, Dong H, Lv X, Bai C, Hu N, Wen L, Yang Z (2018) The adhesion, stability, and electronic structure of  $\gamma$ -TiAl/VN interface: a first-principle study. *Applied Physics A* 124:531
- Yang B, Peng X, Huang C, Yin D, Xiang H, Fu T (2018) Higher strength and Ductility than diamond: nanotwinned diamond/cubic boron nitride multilayer. *ACS applied materials & interfaces* 10:42804–42811
- Bian J, Niu X, Zhang H, Wang G (2014) Atomistic deformation mechanisms in twinned copper nanospheres. *Nanoscale Res Lett* 9:335
- Wang W, Li S, Min J, Yi C, Zhan Y, Li M (2014) Nanoindentation experiments for single-layer rectangular graphene films: a molecular dynamics study. *Nanoscale Res Lett* 9:41
- Sandoval L, Urbassek HM (2015) Collision-spike Sputtering of Au Nanoparticles. *Nanoscale Res Lett* 10:1009
- Yuan Y, Zhang J, Sun T, Liu C, Geng Y, Yan Y, Jin P (2015) Crystallographic orientation-dependent pattern replication in direct imprint of aluminum nanostructures. *Nanoscale Res Lett* 10:96
- Weng S, Ning H, Fu T, Hu N, Wang S, Huang K, Peng X, Qi HJ, Yan C (2019) Anisotropic and asymmetric deformation mechanisms of nanolaminated graphene/Cu composites. *Nano Materials Science* 1:121–130
- Fu T, Peng X, Feng C, Zhao Y, Wang Z (2015) MD simulation of growth of Pd on Cu (1 1 1) and Cu on Pd (1 1 1) substrates. *Applied Surface Science* 356:651–658
- Zhang L, Wu Y, Yu W, Shen S (2019) Response of <110> symmetric tilt grain boundary in titanium nitride under shear. *Engineering Analysis with Boundary Elements* 105:231–241
- Zhang L, Wang L, Yu W, Shen S, Fu T (2019) Structure and shear response of <001> tilt grain boundary in titanium nitride. *Ceramics International* 45: 5531–5546
- Yan G, Yu W, Shen S (2019) High-temperature nanoindentation for temperature-dependent mechanical behavior of enamel coating. *Surface and Coatings Technology* 374:541–548
- Sutrakar VK, Mahapatra DR (2009) Stress-induced martensitic phase transformation in Cu–Zr nanowires. *Materials Letters* 63:1289–1292
- Sutrakar VK, Mahapatra DR (2011) Designing copper–zirconium based nanowires for improving yield strength and plasticity by configuring surface atoms. *Journal of Nanoparticle Research* 13:6907–6918
- Sutrakar VK, Mahapatra DR (2010) Single and multi-step phase transformation in CuZr nanowire under compressive/tensile loading. *Intermetallics* 18:679–687
- Mendelev MI, Ackland GJ (2007) Development of an interatomic potential for the simulation of phase transformations in zirconium. *Philosophical Magazine Letters* 87:349–359
- Mendelev MI, Kramer MJ, Ott RT, Sordelet DJ, Yagodin D, Popel P (2009) Development of suitable interatomic potentials for simulation of liquid and amorphous Cu–Zr alloys. *Philosophical Magazine* 89:967–987
- Xiong K, Gu JF (2015) Understanding pop-in phenomena in FeNi<sub>3</sub> nanoindentation. *Intermetallics* 67:111–120
- Fu T, Peng XH, Zhao YB, Li TF, Li QB, Wang ZC (2016) Molecular dynamics simulation of deformation twin in rocksalt vanadium nitride. *J Alloy Compd* 675:128–133
- Fu T, Peng XH, Zhao YB, Sun R, Yin DQ, Hu N, Wang ZC (2015) Molecular dynamics simulation of the slip systems in VN. *Rsc Advances* 5:77831–77838
- Sandoval L, Urbassek HM (2009) Transformation pathways in the solid-solid phase transitions of iron nanowires. *Applied Physics Letters* 95:191909
- Daw MS, Baskes MI (1984) Embedded-atom method—derivation and application to impurities, surfaces, and other defects in metals. *Physical Review B* 29:6443–6453
- Wang L, Yu W, Shen S, (2019) Revisiting the structures and energies of silicon  $\hat{a}(110)$  symmetric tilt grain boundaries, *J Mater Res*, 34: 1021–1033.
- Wu L, Yu W, Hu S, Shen S (2018) Radiation response of nanotwinned Cu under multiple-collision cascades. *Journal of Nuclear Materials* 505:183–192
- Yu WS, Shen SP, Liu YL, Han WZ (2017) Nonhysteretic superelasticity and strain hardening in a copper bicrystal with a  $\Sigma\{112\}$  twin boundary. *Acta Materialia* 124:30–36
- Wu LP, Yu WS, Hu SL, Shen SP (2017) Stability of stacking fault tetrahedron in twin boundary bicrystal copper under shear. *Int J Plasticity* 97:246–258
- Yu WS, Shen SP (2016) Energetics of point defect interacting with grain boundaries undergone plastic deformations. *Int J Plasticity* 85:93–109
- Borovikov V, Mendelev MI, King AH (2016) Effects of stable and unstable stacking fault energy on dislocation nucleation in nano-crystalline metals. *Model Simul Mater Sci* 24:085017

48. Fu T, Zhang ZJ, Peng XH, Weng SY, Miao YH, Zhao YB, Fu SY, Hu N (2019) Effects of modulation periods on mechanical properties of V/VN nanomultilayers. *Ceramics Int* 45:10295–10303
49. Fu T, Peng XH, Huang C, Weng SY, Zhao YB, Wan ZC, Hu N (2017) Strain rate dependence of tension and compression behavior in nanopolycrystalline vanadium nitride. *Ceramics Int* 43:11635–11641
50. Hoover WG (1986) Constant-pressure equations of motion. *Physical Review A* 34:2499–2500
51. Honeycutt JD, Andersen HC (1987) Molecular-dynamics study of melting and freezing of small Lennard-Jones clusters. *J Phys Chem* 91:4950–4963
52. Larsen PM, Schmidt S, Schiøtz J (2016) Robust structural identification via polyhedral template matching. *Model Simul Mater Sci* 24:055007
53. Kelchner CL, Plimpton SJ, Hamilton JC (1998) Dislocation nucleation and defect structure during surface indentation. *Phys Rev B* 58:11085–11088
54. Stukowski A (2012) Structure identification methods for atomistic simulations of crystalline materials. *Modelling and Simulation in Materials Science and Engineering* 20:045021
55. Xue P, Huang YJ, Pauly S, Jiang SS, Guo S, Fan HB, Ning ZL, Cao FY, Sun JF (2019) Quantitatively determining the martensitic transformation in a CuZr-based bulk metallic glass composite. *J Alloys Compd* 782:961–966
56. Salehinia I, Bahr DF (2014) Crystal orientation effect on dislocation nucleation and multiplication in FCC single crystal under uniaxial loading. *Int J Plasticity* 52:133–146
57. Fu T, Peng XH, Huang C, Zhao YB, Weng SY, Chen X, Hu N (2017) Effects of twin boundaries in vanadium nitride films subjected to tensile/compressive deformations. *Applied Surface Science* 426:262–270
58. An M, Deng Q, Li Y, Song H, Su M, Cai J (2017) Molecular dynamics study of tension-compression asymmetry of nanocrystal  $\alpha$ -Ti with stacking fault. *Materials & Design* 127:204–214
59. Xie HX, Yu T, Yin FX (2014) Tension-compression asymmetry in homogeneous dislocation nucleation stress of single crystals Cu, Au, Ni and Ni<sub>3</sub>Al. *Mat Sci Eng a-Struct* 604:142–147
60. Stukowski A, Bulatov VV, Arsenlis A (2012) Automated identification and indexing of dislocations in crystal interfaces. *Model Simul Mater Sci* 20:085007

### Publisher's Note

Springer Nature remains neutral with regard to jurisdictional claims in published maps and institutional affiliations.

Submit your manuscript to a SpringerOpen<sup>®</sup> journal and benefit from:

- Convenient online submission
- Rigorous peer review
- Open access: articles freely available online
- High visibility within the field
- Retaining the copyright to your article

---

Submit your next manuscript at ► [springeropen.com](https://www.springeropen.com)

---